Insights into the Voltammetry of Cavity Microelectrodes Filled with Metal Powders: The Value of Square Wave Voltammetry

Encarnación Torralba, Eduardo Laborda, Angela Molina, Christine Cachet-Vivier, Stéphane Bastide

Table of Contents/Graphical Abstract

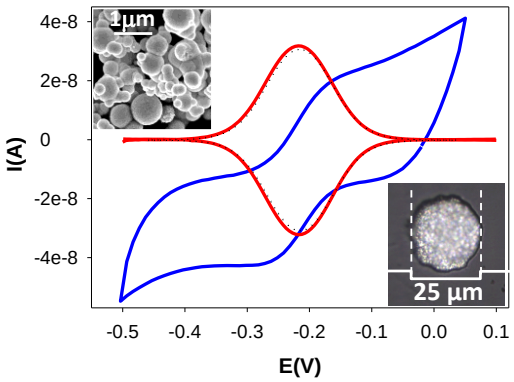

Cyclic and Square Wave Voltammetry for the reduction of $Ru(NH_3)_6^{3+}$ with a Cavity MicroElectrode filled with large surface area platinum powders. SWV supress effectively non faradaic distortions, being advantageous over CV to discriminate faradaic processes. Equations describing SWV responses at CMEs are derived for first time.

Insights into the Voltammetry of Cavity Microelectrodes Filled with Metal Powders: The Value of Square Wave Voltammetry

Encarnación Torralba[a]*, Eduardo Laborda[b], Angela Molina[b], Christine Cachet-Vivier[a], Stéphane Bastide[a]

[a] Dr. Encarnacion Torralba, Prof. Christine Cachet-Vivier, Dr. Stéphane Bastide, Institut de Chimie et des Matériaux Paris-Est, Université Paris-Est, UMR 7182 CNRS-UPEC, 2 rue H. Dunant, 94320 Thiais, France

[b] Dr. Eduardo Laborda, Prof. Angela Molina, Departamento de Química Física, Facultad de Química, Regional Campus of International Excellence "Campus Mare Nostrum", Universidad de Murcia, 30100 Murcia, Spain

*Corresponding author: torralba-penalver@icmpe.cnrs.fr

Abstract

Cavity MicroElectrodes (CMEs) offer a valuable platform to evaluate the electrocatalytic performance of micro- and nano-particulate materials. The technical factors and physicochemical processes affecting the electrochemical response at CMEs are to be recognized, specifically, the accessibility of redox species to the electrocatalyst surface. With this aim, the voltammetric response of CMEs is investigated through a joint experimental and theoretical approach including a comparative study of cyclic and square wave voltammetry (SWV). Experiments reveal a capacitive distortion of the response that increases with the powder surface area, but with a faradaic response analogous to that of recessed or inlaid microdisks, *i.e.* with electrochemical reactions occurring essentially on the first layer of the powder load. We show that SWV is well suited to discriminate Faradaic processes at CMEs and we present accurate mathematical expressions to describe it. These results provide guidelines for the design and analysis of CME voltammetric measurements.

1. Introduction

Since their introduction in the 1990s, Cavity Microelectrodes (CMEs) have gained interest as practical tools for the electrochemical study of finely dispersed materials of application in several fields, such as energy storage, catalyst characterization, corrosion or biological matter, among others [1–7]. Their key advantages compared to classical powder supports are: (i) no addition of external reagents (*i.e.*, binders, carbon) that can introduce their own contribution to the electrochemical response, (ii) use of minute amounts of material (few tens of ng), which are often synthetized in small quantities by complex synthetic routes, and (iii) low distorted voltammetric signals by the ohmic drop, thanks to their micrometric size and low associated current. Additionally, CMEs are easily prepared, cost-effective and their geometry can be accurately determined: the diameter of the cavity corresponds to the diameter of the wire used for their preparation and the cavity depth can be determined either by means of an optical microscope [8] or from the limiting currents of an empty CME considered as a recessed electrode (bottom of the cavity), in the presence of a suitable redox couple [8].

The CME allows the study of catalysts according to (i) their surface properties and (ii) their response related to one or more species in solution. A few examples are given

by way of illustration. Concerning point (i), Locatelli *et al.* were able to relate the charge measured for hydrogen electrosorption on Pt/C and IrO_2-SnO_2 composites to the quantity of material contained in the cavity, allowing a rapid screening of their intrinsic properties under different formulations[9,10]. Regarding point (ii), some of us have studied the electrochemical response of C/bimetallic composites with respect to urea oxidation [7] and nitrate [5] or CO_2 reduction [4,6], with an emphasis on the evolution of the signal as a function of the catalyst composition. Guilminot *et al.* have shown the interest of the CME compared to the rotating disk electrode for the determination of the electro-active surface of Pt supported by carbon and for the extraction of kinetic parameters of oxygen reduction (from Tafel plots), in the frame of PEMFC applications [11]. The data were corrected using the expressions derived for steady state voltammetry of thin active layers deposited on rotating disk electrodes [12,13].

Despite their relatively wide use, the interpretation of the voltammetric signals of soluble redox species obtained with CMEs remains often qualitative. As far as we know, except for Guilminot's work under specific conditions, there is no comprehensive theory describing the voltammetric response of CMEs and the chief processes underlying it. Besides, only linear sweep voltammetry (LSV) and cyclic voltammetry (CV) have been employed to date. Surprisingly, little attention has been given to pulse techniques such as square wave voltammetry (SWV), which are interesting from a quantitative point of view. Only Terbouche *et al.* reported an electrochemical study based on the combination of CME and SWV. The CME was filled with humic acid–polyaniline emeraldine base composites having a high adsorption capacity of metal ions, for the detection of cadmium and nickel in water upon reduction. The enhanced sensitivities and low detection limits attained (*e.g.* 4.2 $nA/\mu M^{-1}$ and 20 nM, respectively, for Cd^{+2} detection) demonstrate the interest of the combination of the CME and SWV for quantitative analysis [14].

Cyclic SWV (CSWV) brings together the advantages of differential pulse techniques and cyclic voltammetry. That is, it provides easily characterizable peak-shape responses, much less affected by double layer effects than CV and it allows for a comprehensive and fast evaluation of the system under study on account of its cyclic waveform. These features make CSWV very suitable for the quantitative characterization of a wide variety of systems [15].

In this work, we combine experiments and theory to study the electrochemical response obtained in CV and CSWV with CMEs densely filled with a metal powder. We focus on interpreting the intrinsic response of this electrode, *i.e.* the basic diffusional and capacitive phenomena occurring between the powder in the CME and a redox couple in solution, and on developing a comprehensive theory allowing a rigorous exploitation of voltammetric signals. For this purpose, electrochemical signals uncomplicated by adsorption or slow reaction kinetics were considered by selecting $Ru(NH_3)_6$(III)/$Ru(NH_3)_6$(II) and platinum as model redox probe and inert metal powder, respectively. This research was carried with a micro and nanopowder, in order to account for the effect of the particle size.

Experimental results show that CV signals are significantly affected by the particle size of the hosted material. Faradaic currents of CMEs deviate from that obtained with a microdisk in a non-straightforward way, being smaller for micropowders and higher for nanopowders. In addition, non-faradaic currents are much higher (especially for the nanopowder), which causes significant distortions of the voltammetric signals. In this context, we show that the use of differential pulse techniques such as SWV is advantageous, as it greatly eliminates background currents and minimize non-faradaic contributions [16,17]. In a second part of the work, an analytical theoretical solution is introduced for the current-potential response of the CMEs filled with metal powders,

assuming that mass transport at a CME can be modelled on the basis of a shallow recessed microdisk. From there, the SWV equations for CMEs are derived for the first time. The main characteristics in SWV (peak coordinates, half-peak width) are investigated as a function of relevant parameters (cavity diameter and recession depth, square wave frequency and amplitude) and the model is finally validated by comparing theoretical and experimental data obtained under various conditions.

2. Results and discussion

2.1 Physical characterization of P_M and P_N

The morphology and structure of P_M and P_N have been examined by SEM and XRD. Representatives SEM images at different magnifications are given in **Figure 1**. In the case of P_M (**Figure 1a** and **b**), well-defined spherical micro-particles can be observed, with a distribution of diameters ranging between 150 and 900 nm. An average particle size of 250 nm was calculated by image processing (Figure S1 of SI). The nanoparticles of P_N (**Figure 1c** and **d)** present a size distribution ranging from 10 to 20 nm. It is important to note that the particle size of P_N is at least 1 order of magnitude smaller than that of P_M, as clearly evidenced by **Figure 1b** and **d**.

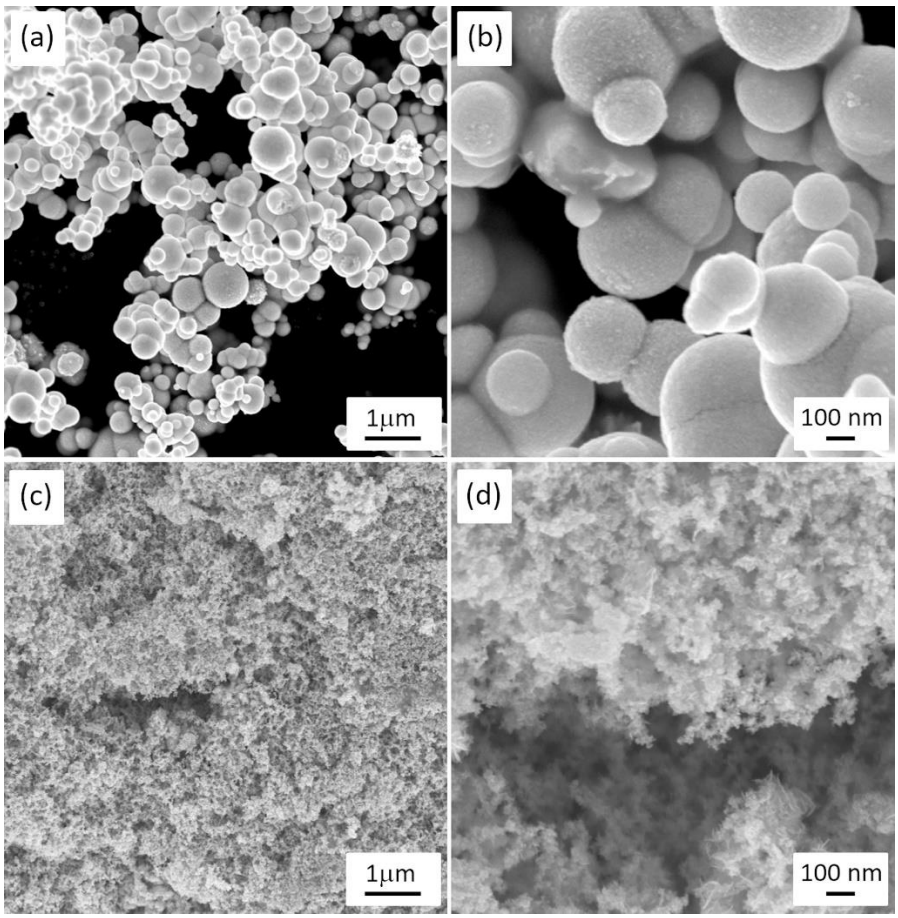

Figure 1. SEM images of P_M (a, b) and P_N (c, d) at two different magnifications.

The XRD patterns of P_M and P_N are given in Figure S2. They show the characteristic diffraction peaks of pure Pt (cubic face centred structure, space group Fm-3m [18]). Unexpectedly, the peak widths are similar for both powders, with an average crystallite size of 9 Å for P_M and 7 Å for P_N (deduced from Scherrer's formula). This means in the case of P_M that the particle size is much higher than the crystallite size (in

accordance with the rather rough aspect of their surface in Figure 1b).

2.2 Electrochemical responses

2.2.1 Cyclic Voltammetry

Figure **2** shows the cyclic voltammograms (CVs) recorded at the CME filled with P_M, P_N and at a Pt microdisk of the same diameter, for the reduction of $[Ru(NH_3)_6]^{3+}$ to $[Ru(NH_3)_6]^{2+}$, under three different sweep rates.

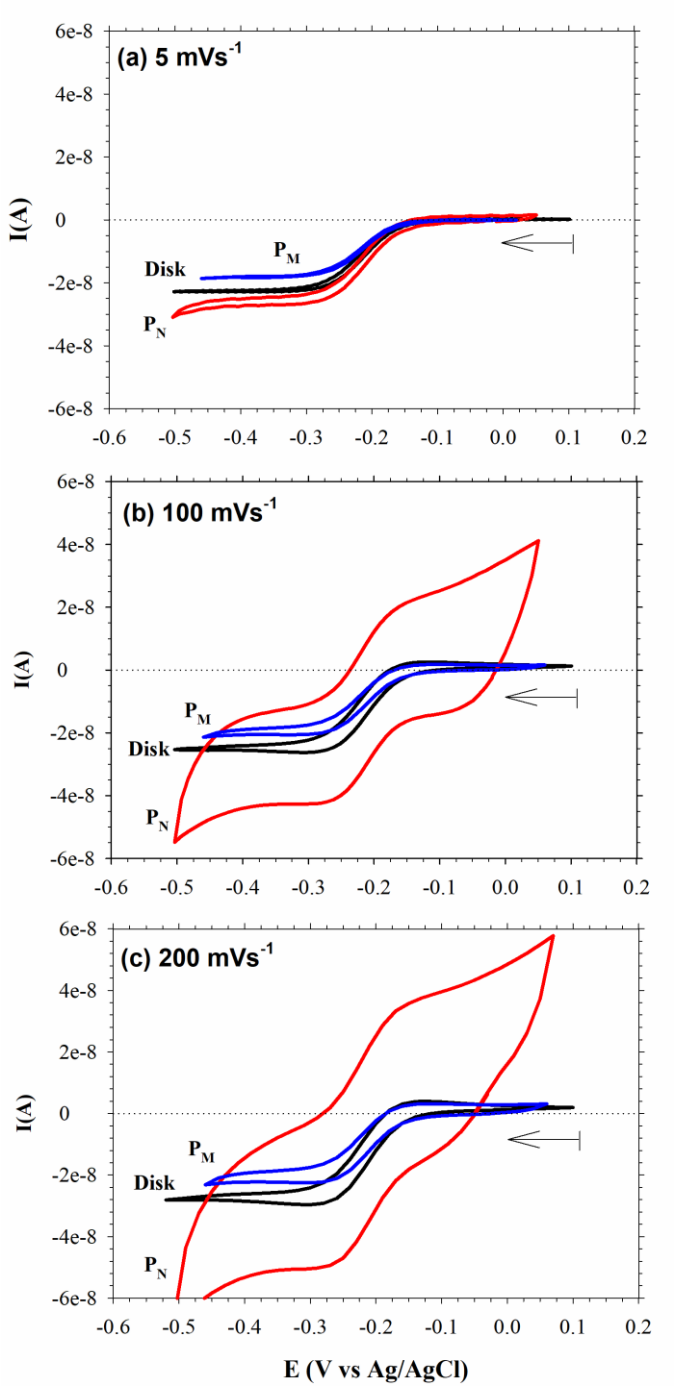

Figure 2. CV responses obtained with the CME filled with P_M and P_N and with a Pt microdisk of the same diameter (25 µm), at three different sweep rates. The initial starting potential and sweep direction are indicated by an arrow. The electrolyte is an aqueous solution of 9 mmol L^{-1} $[Ru(NH_3)_6]Cl_3$ and 0.5 mol L^{-1} K_2SO_4, kept under Ar atmosphere.

At the lowest sweep rate (a - 5 mV s^{-1}), the three CVs (P_M, P_N and Disk) show the sigmoidal form typical of quasi-steady state voltammetry. In such a case, radial diffusion dominates *vs.* planar diffusion (*cf.* Scheme 1a), *i.e.* the condition $r_d^2/D << RT/Fv$ is fulfilled (with r_d, D and v being the radii of the electrode, the diffusion coefficient of $[Ru(NH_3)_6]^{3+}$ and the sweep rate, respectively; R, T and F have their usual meaning) [19]. With P_N, the cathodic and anodic branches do not overlap due to a capacitive current component; a beginning of water reduction is also observed, probably due to a high catalytic activity of Pt nanoparticles.

At higher sweep rates (b - 100 mV s^{-1} and c - 200 mV s^{-1}), the CVs obtained with P_M and the Pt microdisk exhibit a transient character, *i.e.* the signal in the forward and reverse scans do not overlap, the former exhibiting a slightly peaked shape (in this case, $r_d^2/D \sim RT/Fv$ [19]). In comparison, the CVs of P_N exhibit a high capacitive distortion. CV measurements were performed in the absence of redox species to calculate the double layer capacity of P_M and P_N by means of I vs v plots at different scan rates (*cf.* Figure S3 of SI). The CVs confirm that the distortion observed for P_N is due to double layer charging *i.e.* surface area related, its double layer capacity being almost 10 times higher than that of P_M (3.4×10^{-9} F *vs.* 4.3×10^{-8} F, respectively). These differences in capacity imply that the surface of the powders is not smooth and impermeable but presents a certain degree of wettability, *i.e.* that pores of the powder are filled by the electrolyte within a certain depth. A reduction in particle size can thus result in an increased contact area with the electrolyte leading to very significant non-Faradaic currents. In the case of P_N, this causes a distortion of the signals, more apparent when the sweep rate increases. Note that the double layer capacity of P_M is already 34 times higher than that of the Pt microdisk (1×10^{-10} F, based on the 20 µF/cm^2 reported for flat Pt [20]), which should be due to electrolyte filling the pores of the powder as well as to the particle roughness (*cf.* SEM image of Figure 1b).

With respect to Faradaic processes, Figure 2a shows that the steady state limiting current recorded with P_M is slightly smaller than that obtained with the Pt microdisk, while that recorded with P_N is slightly higher. These close values suggest that the redox species are rather electrolyzed at the very surface of the CME [21]. Evidently, such differences (-10 % with P_M and +10 % with P_N) point out a significant divergence between the behavior of CME and microdisk electrodes. With regard to P_M, we hypothesize that the difference observed between the steady state Faradaic limiting current of P_M and the microdisk should be related to the features of the mass transport towards the surface of the CME load. In this sense, the smaller steady state current provided by P_M can point out that the powder is recessed in the cavity, as schemed in Figure 3c so that diffusion of the electroactive species towards the powder surface area is less effective since the quasi-linear diffusion inside the top part of the cavity acts as a 'bottleneck' [22]: the deeper the recess, the stronger the mass transfer limitation.

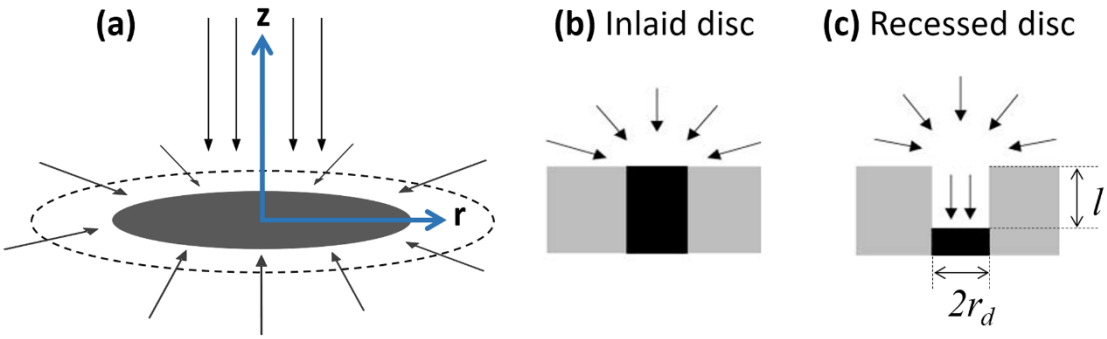

Figure 3. Schematic views of: (a) the radial, r, and planar, z, diffusion fields at a microdisk electrode; (b) an inlaid and (c) a recessed microdisk.

The above hypothesis was first verified via the optical images presented in Figure 4. The CME filled with P_M appears moderately recessed, with a recession length *l* between 2.8 and 3.2 µm (difference in z values obtained when focusing on the middle of the CME and on the glass just outside the cavity). On the contrary, the CME is completely filled in the case of P_N (with a slightly crowned inner rim on one side).

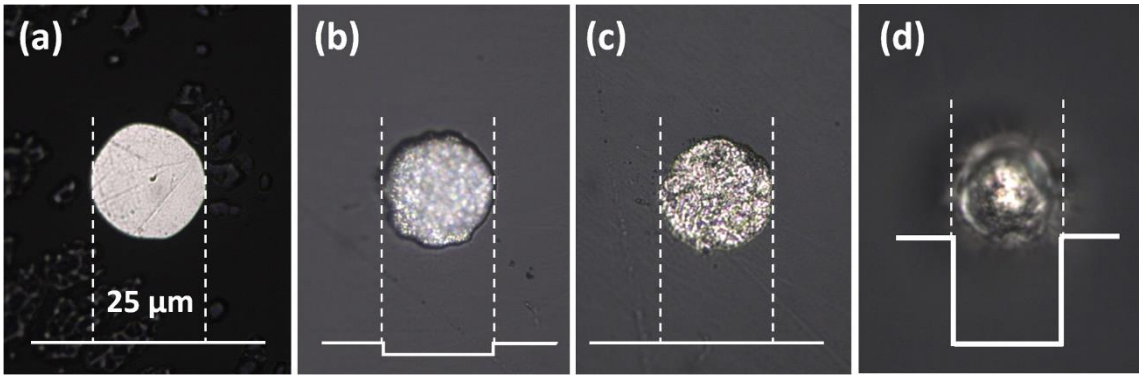

Figure 4. Optical microscopy images of the Pt microdisk electrode (a), the CME filled with P_M (b) and with P_N (c), the empty CME (d).

The recession depth was also estimated from the theoretical expression of the steady state limiting current for a recessed microdisk [16]:

$$I^{ss}_{lim,recessed} = FADc^{*}_{O}\frac{4}{4l+\pi r_d} \qquad (1)$$

where *A* represents the geometrical area of the microdisk opening, *l* the recession depth, *Co** the bulk concentration of the electroactive specie and *D* its diffusion coefficient. From the I^{ss}_{lim} value measured with P_M at 5 mV s^{-1} and a *D* value for $[Ru(NH_3)_6]^{3+}$ of 5.2 10^{-6} cm^2s^{-1} (obtained experimentally from the I^{ss}_{lim} value measured with the microdisk at 5 mVs^{-1} and Eq.(1) with l = 0 [16] and in good agreement with the literature [23]) a recession depth of 2.4 µm is found, which is close to the values obtained by optical microscopy. Thus, optical microscopy and electrochemical data point out that the CME filled with P_M can be considered a recessed microdisk.

Taking into account the results presented above, we propose that the Faradaic response of the CME can be modelled (in first approach and for the metallic powders studied here) as that of a microdisk electrode, inlaid or recessed, by assuming that the electrochemical reactions take place essentially on the first layer of the load (*i.e.* two-dimensional rather than three-dimensional electrode). The predictions resulting from this

modelling are given and contrasted with experimental data in section 3.3.

Note that a question remains regarding the nanoparticle powder P_N. Its limiting current is higher than that of the microdisk which is difficult to explain with the model proposed. At first instance, the higher current could be attributed to a higher projected area of P_N, due to powder protruding from the microcavity (*i.e.* a higher geometrical area on the cavity surface). However, the SWV signals rule out this hypothesis, showing identical faradaic responses for P_N and the disk (*i.e.* identical surface geometrical areas, see Figure 5). Thus, with the help of the SWV results, we can conclude that the higher steady state current for P_N in CV is indeed an artefact resulting from uncorrected double layer distortion. Overlapping of the end of the reduction wave of $[Ru(NH_3)_6]^{3+}$ with the beginning of that of water reduction is involved as well in the apparent higher steady state current (see Figure 5 for more details).

2.2.2 Cyclic Square Wave Voltammetry

A quantitative analysis of highly distorted CVs to extract relevant parameters of the system, such as E^0, L or Co^*, would require independent baseline corrections or background subtraction of the forward and reverse scans, which can be cumbersome and inaccurate. In this respect, the use of pulsed techniques can be very advantageous [15] since they provide a fast and effective suppression of double layer charging current. In each potential pulse, the charging current associated to the potential change decays with time more rapidly than the Faradaic current. Hence, by using long enough pulse duration and recording the current response at the end of each pulse, the interference of the capacitive signal can be reduced. Among pulse techniques, differential techniques are particularly valuable since their subtractive nature enable further suppression of residual non-Faradaic and Faradaic currents. Accordingly, the use of SWV at CMEs is considered. The SWV method also allows for fast measurements, comparable to sweep techniques. A brief description of the waveform and current response of the SWV technique is given in the section 5 of the supporting information; further information can be obtained in [15–17].

Figure 5 shows the experimental baseline-corrected CSWV responses for the reduction of $[Ru(NH_3)_6]^{+3}$, obtained with the CME filled with P_M and P_N and with the microdisk electrode, for different square wave amplitudes E_{sw} and frequencies f. It is worth noting that the baseline correction in SWV is easier and more precise than in CV, given that there are more guiding criteria to establish a suitable baseline, namely, the corrected response of reversible electron transfers is a symmetric bell-shape peak starting and ending at zero current; also, the peaks in the forward and reverse scans are symmetric (see Section 2.3). To better illustrate this, Figure S4 shows several CSWV curves before and after baseline correction.

As indicated above, the experimental I_{sw}/E curves show two symmetrical bell-shape peaks. The exponential currents before and after the main signal correspond to water reduction/oxidation (limits of the potential window). Note that these signals do not appear for P_M (neither for the Pt microdisk) in the potential window provided in the figure. They appear much later and hence are not shown. This evidence a higher catalytic activity of Pt nanopowders compared to micropowders for water reduction/oxidation, which can also contribute to the higher limiting currents displayed by P_N in CV.

For moderate values of E_{sw} and f (**Figure 5 a, b** and **d, e**), the anodic and cathodic branches of the SWVs are symmetrical, exhibiting no capacitive distortion. The peak current obtained with P_M is lower than that obtained with the microdisk, which agrees with the smaller limiting current observed in CV and is consistent with the fact that the powder is recessed in the cavity (see Section 2.3). In turn, the peak current provided for P_N overlaps with the value obtained with the microdisk (especially for the cathodic scan),

i.e. the two electrodes provided the same faradaic current for $[Ru(NH_3)_6]^{+3}$ reduction, hence identical geometrical surfaces contributing to the faradaic process. Our assumption that the electrochemical reactions take place essentially on the first layer of the CME load is consistent with these observations. Thus, we can conclude that for typical values of E_{sw} and f, the curves in SWV are adequate for a quantitative analysis. For larger values of E_{sw} and f (*e.g.* f = 25 Hz, corresponding to a pulse time as small as 0.02 s) the double-layer current with P_N is very significant, and its suppression is not effective, even with this technique.

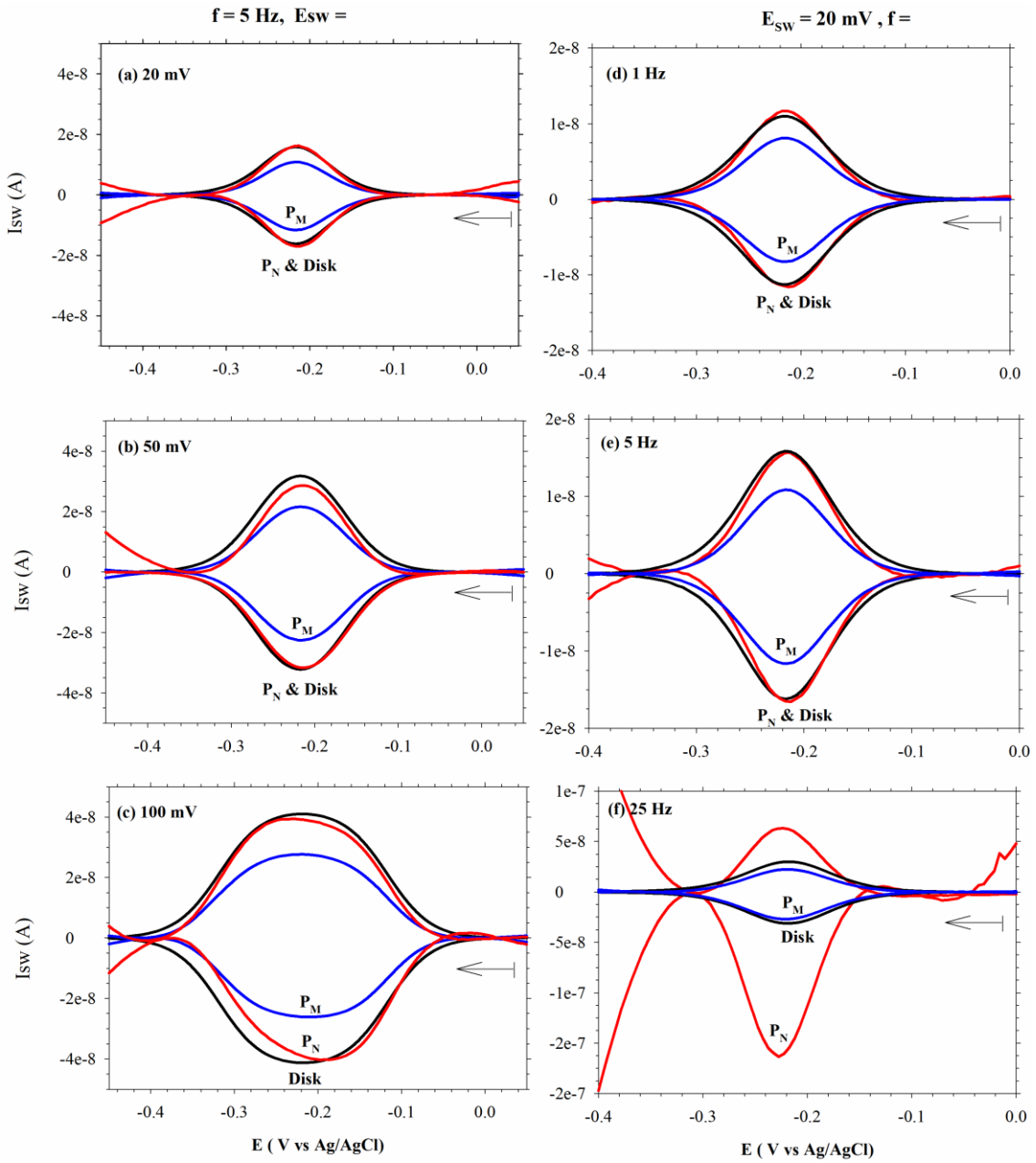

Figure 5. Baseline corrected CSWVs obtained with the CME filled with P_M (blue line) and P_N (red line) and with a Pt microdisk (black line) at different amplitudes E_{sw} (left column) and frequencies, f (right column). Electrolyte: aqueous solution of 9 mM $[Ru(NH_3)_6]Cl_3$ and 0.5 mol L^{-1} in K_2SO_4. Argon atmosphere. Technique parameters: Es = 5 mV for all figures, f = 5 Hz for (a) - (c), E_{sw} = 20mV for (d) – (f). The initial potential and sweep direction is indicated by an arrow.

2.3 Theoretical description of the SWV responses

Under the assumption that the flux of electroactive species towards the CME in the experimental conditions here considered is equivalent to that towards an inlaid or a shallow recessed microdisk, the following equation is deduced for the theoretical Faradaic SWV response of reversible electron transfers (see section 5 in the supporting information for the derivation):

$$I_{SW,\gamma} = FAD\left\{\left(c_O^{s,2\gamma} - c_O^{s,2\gamma-1}\right) f_G^1 + \sum_{m=1}^{2\gamma-1}\left(c_O^{s,m-1} - c_O^{s,m}\right)\left(f_G^{2\gamma-m} - f_G^{2\gamma-m+1}\right)\right\} \qquad (\gamma = 1,\ 2,\ \ldots np/2) \tag{2}$$

where γ refers to the γ-th SW cycle (see SI) and $c_O^{s,p}$ to the surface concentration of the oxidized species, which is demonstrated to be only dependent on the applied potential in any pulse *p* [24]:

$$\begin{aligned} c_O^{s,0} &= c_O^* \\ c_O^{s,p} &= c_O^*\left(\frac{e^{\eta_p}}{1+e^{\eta_p}}\right) \quad \text{for } p > 0 \end{aligned} \tag{3}$$

with:

$$\eta_p = \frac{F}{RT}\left(E_p - E^{0'}\right) \quad \text{for } p > 0 \tag{4}$$

The function f_G^λ depends on time and the geometry of the electrode [24]; thus, the expressions for inlaid and shallow recessed microdisks of radius r_d are given by:

$$f_{inlaid}^\lambda = \frac{4}{\pi r_d}\left(0.7854 + 0.44315\frac{r_d}{\sqrt{D\lambda\tau}} + 0.2146\exp\left(-0.39115\frac{r_d}{\sqrt{D\lambda\tau}}\right)\right) \tag{5}$$

$$f_{recessed}^\lambda = B\frac{r_d}{\sqrt{D\lambda\tau}} + C\exp\left(-D\frac{r_d}{\sqrt{D\lambda\tau}}\right) \tag{6}$$

where τ is the pulse duration ($\tau = \frac{1}{2f}$, see SI) and the values of *B*, *C* and *D* depend on the recess depth as given in [25].

In **Figure 6**, the influence of the cavity radius and the recess depth ($L = l / r_d$) on the SWV signal is studied using Eq. (2). In all cases, bell-shape signals of the same half-peak width are obtained irrespective of the electrode geometry and under both transient and steady state conditions. For a very large cavity (Figure 6**a**), edge effects are negligible (linear diffusion prevails) and diffusion conditions are equivalent at both inlaid and recessed electrodes; accordingly, the SWV curves do not depend on the L-value. In Figure 6**b**, conditions similar to those of the experimental study with CME are considered: f = 20 Hz, r_d = 12.5 μm and L ranges between 0 and 0.3. In this case, the effect of the recession of the powder is apparent, so that the larger the recession depth, the smaller the peak current. However, the peak shape, width and position are unaffected. For smaller cavity radius (*i.e.* ultramicrocavity electrodes, Figure 6c), steady state conditions are attained, which can be inferred from the sigmoidal shape of the signal components (see Figure S5 of SI for more details).

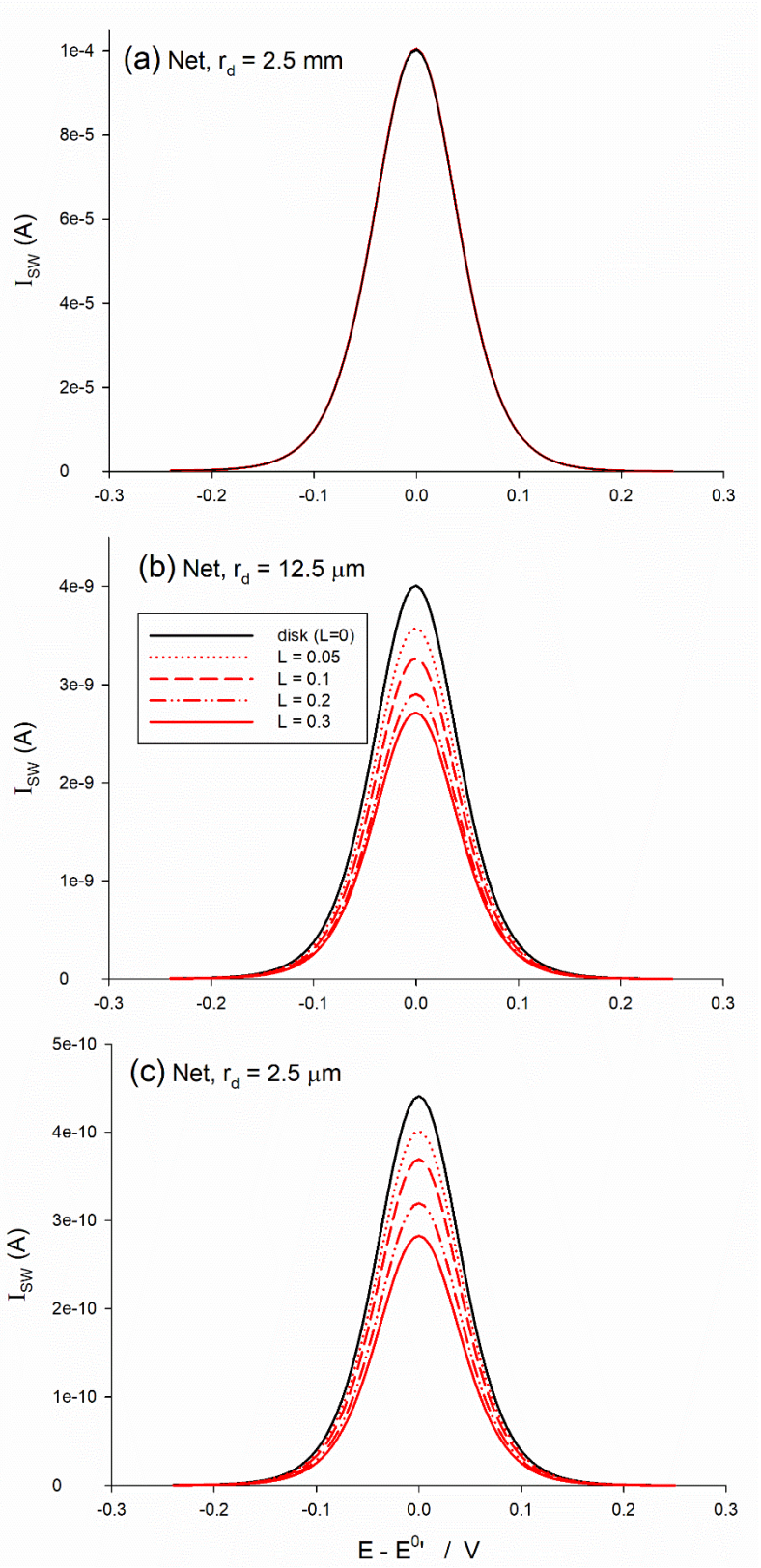

Figure 6. Theoretical SWVs as a function of the recess depth L and the radius of the cavity r_d: 2.5 mm (a), 12.5 µm (b) and 2.5 µm (c). E_{sw} = 20 mV, E_s = 5 mV, f = 20 Hz.

Under steady state conditions, the functions f_G^{λ} become time-independent and Eq. (2) simplifies to:

$$\text{inlaid:}\quad I_{SW,y}^{ss} = FAD\left(c_O^{s,2y} - c_O^{s,2y-1}\right)\frac{4}{\pi r_d} \qquad (y = 1,\ 2,\ \ldots np/2)$$

$$\text{recessed:}\ I_{SW,y}^{ss} = FAD\left(c_O^{s,2y} - c_O^{s,2y-1}\right)\frac{4}{4l + \pi r_d} \qquad (y = 1,\ 2,\ \ldots np/2) \tag{7}$$

from which the following simple expressions are derived for the peak currents:

$$\text{inlaid:}\quad I_{SW,peak}^{ss} = FADc_O^{*}\frac{4}{\pi r_d}\tanh\left(\frac{FE_{SW}}{2RT}\right)$$

$$\text{recessed:}\ I_{SW,peak}^{ss} = FADc_O^{*}\frac{4}{4l + \pi r_d}\tanh\left(\frac{FE_{SW}}{2RT}\right) \tag{8}$$

In all cases, the half-peak width is given by:

$$W_{1/2} = \frac{RT}{F}ln\left(\frac{1 + e^{2\eta_{sw}} + 4e^{\eta_{sw}} + \sqrt{\left(1 + e^{2\eta_{sw}} + 4e^{\eta_{sw}}\right)^2 - 4e^{2\eta_{sw}}}}{1 + e^{2\eta_{sw}} + 4e^{\eta_{sw}} - \sqrt{\left(1 + e^{2\eta_{sw}} + 4e^{\eta_{sw}}\right)^2 - 4e^{2\eta_{sw}}}}\right) \tag{9}$$

with $\eta_{SW} = FE_{SW}/RT$, and the potential peak is centred at the half-wave potential of the system, $E^{1/2}$ [17]:

$$E_{peak}^{ss} = E^{1/2} = E^{0'} + \frac{RT}{F}ln\left(\frac{D_{red}}{D}\right) \tag{10}$$

When $D_{red} \sim D$, the potential peak coincides with the formal reduction potential $E^{0'}$.

Two important technique parameters in SWV are the SW frequency (f) and the square wave amplitude (E_{SW}). Their effects on the theoretical SWV response provided by the CME are shown in Figures S6 and S7 of the SI. Essentially, f affects the intensity of the signals (peak current) while E_{sw} affects the intensity and width of the peak. With respect to the frequency effect, $I_{SW,peak}$ scales linearly with $f^{1/2}$ when linear diffusion domains (i.e, for large cavities), a nonlinear increase is predicted for micro-cavities (due to convergent diffusion) and no dependence is predicted for ultramicrocavities (*i.e.* constant value of $I_{SW,peak}$) due to the attainment of the steady state (Figure S6). As for E_{sw}, its increase causes an increase of the peak current and a broadening of the SWV signals, so that the well-defined peak at small E_{SW}-values eventually turns into a *plateau* (Figure S7 and Figure 5c). The equations characterizing this current plateau are derived in the supporting info. It is noteworthy that no effect of f or E_{sw} is predicted in the peak position. The peaks are centered around the formal potential whatever the values of E_{SW} and f are (not shown). Hence, if experimental SWV curves show peaks of different magnitude and position in the forward and reverse scans, this will be indicative of complications related to, for example, sluggish electron transfers, capacitive distortions or ohmic drop.

Figure 7 shows the experimental SWV signals (same as in Figure 5) together with the theoretical ones (dotted lines), obtained with the equations here derived for the CME (Eq. (2)), by using the formal potential, $E^{0'}$, and the dimensionless recession depth, L, as the two only adjustable parameters. $E^{0'}$ determines the peak position and L the peak height, as explained in Figure 6. As can be seen, a very good agreement between theoretical and experimental data is reached, not only at the peak region but for the whole curve, with the exception of the extreme case f = 25 Hz (Figure 7f). The experimental SWVs follow the trend described theoretically with f and E_{sw}, *i.e.* the current peak increases with both parameters, and the peak broadens with E_{sw} and becomes a plateau for $E_{sw} \geq 100$ mV (Figure 7c). The good agreement between theoretical and experimental data in a variety of conditions supports the consistency of the model and the

corresponding equations deduced.

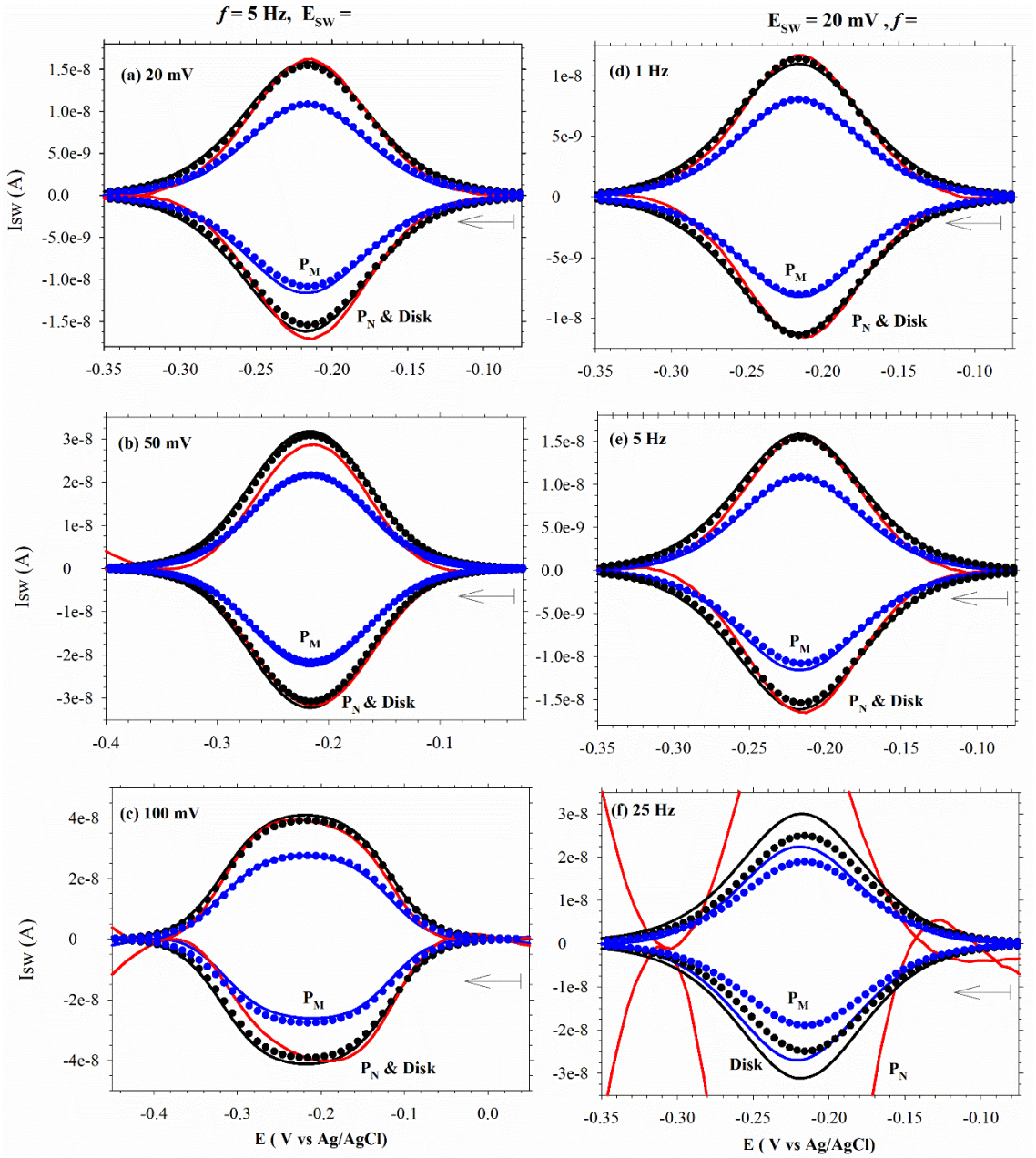

Figure 7. Experimental (lines) and best-fit theoretical (points) cSWV responses corresponding to the conditions considered in figure 5.

The fittings of the experimental curves yield an optimal value of the apparent $E^{0'}$ of -0.216 V *vs.* Ag/AgCl (3 M KCl), identical for P_M, P_N and the disk, and in agreement with the literature [23]. A value of $L = 0.21$ was obtained from the fitting of the SWVs obtained with P_M. This yields a value for the recession depth of the CME filled with Pt microparticles of $l = 2.6$ µm, with matches the values obtained by CV and optical imaging (see Section .2.1). Finally, the agreement between theoretical and experimental responses, specifically in terms of the peak width, show that the system behaves as reversible (as reported in [23]) with both P_M and P_N. Thus, the particle size of the powder has no effect on the interfacial charge transfer rate of the $[Ru(NH_3)_6]^{2+/3+}$ system.Otherwise, the

broadening of the SWV peaks would have occurred [15,17].

3. Conclusions

The CME combined with SWV offers a very convenient approach to study the electrochemical properties of metal powders. In this work, the voltammetric response of CMEs densely filled with Pt powders has been investigated by joint experimental and theoretical approaches including a comparative study of CV and SWV, optical imaging, and theoretical modelling. Particular attention has been paid to highlighting and interpreting the influence of the grain size of the hosted powder on the voltammetric response as well as to developing a comprehensive theory enabling their quantitative exploitation. Strong signal distortions are found in the CVs of ultrafine powders, due to non-faradaic currents (double layer charging currents) resulting from partial penetration of the electrolyte in the cavity. On the contrary, well-defined peak-shape signals, much less affected by charging effects are obtained with SWV. Thus, this technique avoids the important capacitive distortions observed in CV. With respect to electrolyte-related Faradaic processes, we have demonstrated that the behavior of the powder-filled CME is actually similar to that of a shallow recess or inlaid microdisk (depending on the particle size), with redox species being electrolyzed on the outer surface of the powder. On this basis, simple mathematical expressions have been derived for data analysis, which provide information on the geometry of the cavity (diameter and recess depth) and on the electron transfer.

The CME filled with metal particles therefore presents an electrochemical response that is well understood and modelled. Hence, it appears as a tool of choice in the direct and rapid investigation of the electrocatalytic properties of pure metals or metal compounds synthesized in powder form.

4. Experimental

4.1 Hosted powders

Pt particles in the micrometer and nanometer range (P_M and P_N, hereafter) were used as hosted powders. The first was a commercial powder purchased from Acros Organics, while the second was synthetized in our laboratory (see below).

4.2 Synthesis of Pt nanoparticles.

Pt nanoparticles (P_N) were synthetized by a soft chemical route in aqueous media, using $H_2PtCl_6 \cdot 6H_2O$ as metal salt precursor and $NaBH_4$ as reducing agent (from Sigma-Aldrich and Prolabo, respectively). First, 0.5 mmol of $H_2PtCl_6 \cdot 6H_2O$ were dissolved in 150 mL of 0.05 mol L^{-1} H_2SO_4 (pH = 1) at ~ 0°C (ice bath) and degassed with argon for 30 minutes under constant stirring. Second, 50 mL of 10 mmol L^{-1} $NaBH_4$ (at ~ 0°C) were poured at once in the metal precursor solution under vigorous stirring for one hour (under argon atmosphere) to ensure completion of the reaction.

The powder obtained was collected by centrifugation/decantation and washed 5 times with ultra-pure water and 5 times with absolute ethanol. The precipitate was then sonicated with the minimum quantity of ethanol (*ca.* 150 - 200 µL) during 5 min to avoid powder agglomeration, then left to dry under primary vacuum and stored under vacuum. The Pt yield was 93 wt.%.

4.3 Physical characterisation

Structural characterization of P_M and P_N was performed by X-Ray diffraction (XRD) using a D8 advanced Bruker diffractometer (copper K radiation). The software EVA was used for XRD data processing. CellRef and EVA were used to obtain the values of the lattice parameter and crystallite size (Scherrer equation), respectively. The powder

morphology was observed by Scanning Electron Microscopy (SEM) with a Merlin FEG microscope from Zeiss. The particle size was determined from SEM images using the software ImageJ.

4.4 Electrochemical measurements

A three-electrode cell (50 mL) was used to carry out the electrochemical measurements with an Autolab PGSTAT 30 potentiostat from Metrohm equipped with the software NOVA.

The working electrode was a homemade cavity microelectrode (CME). It consists of a Pt wire embedded in a glass rod with a cavity at the tip of 25 µm in diameter and 20 µm in depth (the bottom of the cavity corresponds to the end of the Pt wire). The cavity has an opening area of 4.9 10^{-6} cm^2 and a volume of ~ 10^{-7} cm^3. Fabrication and use of CMEs are described in more detail in [8]. A Pt wire was used as counter electrode and an Ag/AgCl (3 M KCl) electrode as reference (E = 0.209 V vs. SHE). The CME was filled with the powder material by simple mechanical pressure of the electrode tip against the powder. It was emptied electrochemically as follows: for P_M, the Pt powder was electrochemically dissolved by immersing the CME in a saturated solution of $CaCl_2$ in acetone/water 50/50 V/V and applying a sinusoidal voltage (50 Hz frequency and 20 V peak-to-peak amplitude) during 20 s. A TG550 Function Generator from Thurlby Thandar Instruments was used for this purpose. For P_N, the powder was ejected from the cavity by forced HER at potentials up to -3 V. CV and CSWV were performed in a solution of 9 mM of $[Ru(NH_3)_6]Cl_3$ (Sigma-Aldrich) in 0.5 mol L^{-1} K_2SO_4, at room temperature. Before each experiment, 30 mL of this solution were purged with Ar for 10 min. Ar atmosphere was maintained throughout the experiments. A Pt microdisk electrode (CH Instruments), 25 µm in diameter, was used as working electrode for the sake of comparison. Before each measurement, it was polished with a diamond paste (1µm), an alumina paste (0.3 µm), then sonicated in water/ethanol 50:50 (v:v) for 1 minute and rinsed with water.

The analytical theoretical solutions for the CSWV Faradaic responses at inlaid and recessed microdisks were implemented in homemade C++ programs available upon request.

Acknowledgements

AM and EL greatly thank the financial support provided by the Fundacion Séneca de la Región de Murcia (Project 19887/GERM/15) and by Ministerio de Economía y Competitividad (PID2019-106097GB-I00). ETP, CCV and SB thank ICMPE, CNRS and UPEC for financial supports.

Keywords: cavity microelectrode, cyclic voltammetry, electrocatalysis, nanoparticles, square wave voltammetry

References

[1] D. Gruet, B. Delobel, D. Sicsic, I. T. Lucas, M. Turmine, V. Vivier, *Electrochem. Commun.* **2018**, *95*, 23–27.

[2] E. Mourad, O. Fontaine, *J. Mater. Chem. A* **2019**, *7*, 13382–13388.

[3] E. R. Bertelsen, N. C. Kovach, B. G. Trewyn, M. R. Antonio, J. C. Shafer, *J. Mater. Chem. C* **2020**, *8*, 6689–6700.

[4] E. Torralba, N. Blanchard, C. Cachet-Vivier, D. Muller-Bouvet, J. González, S. Bastide, *Electrochim. Acta* **2020**, *354*, 136739.
[5] P. Mirzaei, S. Bastide, A. Aghajani, J. Bourgon, C. Zlotea, M. Laurent, M. Latroche, C. Cachet-Vivier, *Electrocatalysis* **2018**, *9*, 343–351.
[6] Z. Bitar, A. Fecant, E. Trela-Baudot, S. Chardon-Noblat, D. Pasquier, *Appl. Catal., B* **2016**, *189*, 172–180.
[7] P. Mirzaei, S. Bastide, A. Dassy, R. Bensimon, J. Bourgon, A. Aghajani, C. Zlotea, D. Muller-Bouvet, C. Cachet-Vivier, *Electrochim. Acta* **2019**, *297*, 715–724.
[8] C. Cachet-Vivier, M. Keddam, V. Vivier, L. T. Yu, *J. Electroanal. Chem.* **2013**, *688*, 12–19.
[9] C. Locatelli, A. Minguzzi, A. Vertova, P. Cava, S. Rondinini, *Anal. Chem.* **2011**, *83*, 2819–2823.
[10] A. Minguzzi, C. Locatelli, G. Cappelletti, C. L. Bianchi, A. Vertova, S. Ardizzone, S. Rondinini, *J. Mater. Chem.* **2012**, *22*, 8896–8902.
[11] E. Guilminot, A. Corcella, M. Chatenet, F. Maillard, *J. Electroanal. Chem.* **2007**, *599*, 111–120.
[12] O. Antoine, Y. Bultel, R. Durand, P. Ozil, *Electrochim. Acta* **1998**, *43*, 3681.
[13] F. Gloaguen, F. Andolfatto, R. Durand, P. Ozil, *J. Electroanal. Chem.* **1994**, *24*, 863–869.
[14] A. Terbouche, C. Ait-Ramdane-Terbouche, S. Djebbar, O. Benali-Baitich, D. Hauchard, *Sens. Actuators, B* **2012**, *169*, 297–304.
[15] V. Mirceski, S. Komorsky-Lovric, M. Lovric, *Square-Wave Voltammetry: Theory and Application*, Springer-Verlag, Berlin Heidelberg, **2007**.
[16] B. J. Allen, L. R. Faulkner, Eds. , *Electrochemical Methods: Fundamentals and Applications*, Wiley-VCH, **2000**.
[17] Á. Molina, J. González, *Pulse Voltammetry in Physical Electrochemistry and Electroanalysis*, Springer International Publishing, Cham, **2016**.
[18] H. E. Swanson, *Standard x-ray diffraction powder patterns* **1967**, *25*.
[19] R. G. Compton, C. E. Banks, *Understanding Voltammetry*, Imperial College Press, **2010**.
[20] T. Pajkossy, D. M. Kolb, *Electrochem. Commun.* **2007**, *9*, 1171–1174.
[21] E. Kätelhön, R. G. Compton, *Applied Materials Today* **2020**, *18*, 100514.
[22] D. W. M. Arrigan, *Analyst* **2004**, *129*, 1157.
[23] Y. Wang, J. G. Limon-Petersen, R. G. Compton, *J. Electroanal. Chem.* **2011**, *652*, 13–17.
[24] A. Molina, J. Gonzalez, E. O. Barnes, R. G. Compton, *J. Phys. Chem. C* **2014**, *118*, 346–356.
[25] P. N. Bartlett, S. L. Taylor, *J. Electroanal. Chem.* **1998**, *453*, 49–60.